Solar Phys (2009) 255: 107–118
DOI 10.1007/s11207-009-9316-y

Evaluating Mean Magnetic Field in Flare Loops

Jiong Qiu · Dale E. Gary · Gregory D. Fleishman

Received: 25 August 2008 / Accepted: 7 January 2009 / Published online: 13 February 2009

Abstract We analyze multiple-wavelength observations of a two-ribbon flare exhibiting apparent expansion motion of the flare ribbons in the lower atmosphere and rising motion of X-ray emission at the top of newly-formed flare loops. We evaluate magnetic reconnection rate in terms of $V_r B_r$ by measuring the ribbon-expansion velocity (V_r) and the chromospheric magnetic field (B_r) swept by the ribbons. We also measure the velocity (V_t) of the apparent rising motion of the loop-top X-ray source, and estimate the mean magnetic field (B_t) at the top of newly-formed flare loops using the relation $\langle V_t B_t \rangle \approx \langle V_r B_r \rangle$, namely, conservation of reconnection flux along flare loops. For this flare, B_t is found to be 120 and 60 G, respectively, during two emission peaks five minutes apart in the impulsive phase. An estimate of the magnetic field in flare loops is also achieved by analyzing the microwave and hard X-ray spectral observations, yielding $B = 250$ and 120 G at the two emission peaks, respectively. The measured B from the microwave spectrum is an appropriately-weighted value of magnetic field from the loop top to the loop leg. Therefore, the two methods to evaluate coronal magnetic field in flaring loops produce fully-consistent results in this event.

1. Introduction

Magnetic reconnection is considered to be the driver of solar flares, yet direct observations of magnetic reconnection in the Sun's corona cannot be achieved with existing capabilities because of the very small length scale required for fast reconnection on the observed time scales. However, the consequence of energy release is macroscopic, as reflected in heated plasmas and accelerated particles, which subsequently result in radiations of all sorts. In past decades, observations of solar-flare evolution in multiple

J. Qiu (✉)
Physics Department, Montana State University, Bozeman, MT 59717-3840, USA
e-mail: qiu@physics.montana.edu

D.E. Gary · G.D. Fleishman
Physics Department, New Jersey Institute of Technology, 323 ML King Blvd., Newark, NJ 07102-1982, USA

wavelengths have given rise to the standard flare model (see Forbes and Acton, 1996, and references therein), based on which the rate of magnetic reconnection, an important parameter in evaluating energy release, may be inferred. Observational determination of the reconnection rate has been approached from two avenues. The first is through measurements made by directly observing inflows at the coronal reconnection site, and estimating the inflow Mach number ($M \equiv V_{\rm in}/V_{\rm A}$) with a certain assumption or estimate of coronal magnetic field and plasma density at the reconnection site (Yokoyama *et al.*, 2001; Lin *et al.*, 2005). The second approach derives reconnection rate in terms of reconnecting electric field (in a 2D approximation, but see Lee and Gary, 2008, concerning modifications to 3D) or reconnection flux (in a general configuration) by observing flare evolution in the lower atmosphere (Poletto and Kopp, 1986; Fletcher and Hudson, 2001; Isobe *et al.*, 2002; Isobe, Takasaki, and Shibata, 2005; Qiu *et al.* 2002, 2004; Fletcher, Pollock, and Potts, 2004; Qiu and Yurchyshyn, 2005; Saba, Gaeng, and Tarbell, 2006) from which the energy–release rate can be deduced by assuming a constant Mach number $(M) = 0.01 - 0.1$ (Isobe *et al.*, 2002; Isobe, Takasaki, and Shibata, 2005; Lee, Gary, and Choe, 2006; Temmer *et al.*, 2007; Miklenic *et al.*, 2007).

The second approach is grounded in the principle that magnetic flux is conserved from the corona to the photosphere along a given field line, and the field lines that participate in reconnection become "visible" as X-ray or EUV flare loops and Hα or UV ribbons because of instantaneous energy release along these field lines. Suppose reconnection proceeds over time τ, and total reconnection flux is equivalent to the flux swept up by flare ribbons (subscript r) in the lower atmosphere as $\Phi_{\rm r} = V_{\rm r} B_{\rm r} \tau L_r$. In the meantime, magnetic reconnection will form closed flare loops, and the total amount of flux closed into flare loops is $\Phi_{\rm t} = \int B_{\rm t} L_{\rm t}\, {\rm d}H \approx \langle B_{\rm t}\rangle \langle V_{\rm t}\rangle \tau L_{\rm t}$, where $V_{\rm t}$ is the speed of "growth" of the loop top (subscript t), which can be inferred from the apparent rising motion of an emitting source at the loop top. This apparent growth is due to the fact that plasmas are heated instantaneously at the time of reconnection, which forms new flare loops on top of loops formed earlier. Given that the time τ is greater than typical timescales of reconnection, energy transport along the loop, and plasma heating at all levels of the atmosphere, magnetic flux is conserved from the corona to the photosphere, or $\Phi_{\rm t} = \Phi_{\rm r}$. In a 2.5D approximation, it is also assumed that the length along the arcade is the same in the corona and at the ribbons, $L_{\rm t} = L_{\rm r}$. Therefore, to first order, $\langle V_{\rm r}\rangle \langle B_{\rm r}\rangle \approx \langle V_{\rm t}\rangle \langle B_{\rm t}\rangle$, providing a way to estimate magnetic-field strength $\langle B_{\rm t}\rangle$ at the top of flare loops from measured quantities $\langle V_{\rm r}\rangle$, $\langle B_{\rm r}\rangle$, and $\langle V_{\rm t}\rangle$.

In this paper, we present an experiment to evaluate the mean magnetic-field strength at the top of newly-formed flare loops by analyzing flare evolution at the root and top of the flare loops using the flux-conservation rule. For this purpose, we analyze a two-ribbon flare well observed in the lower atmosphere and the corona in different wavelengths, which exhibits regular motion patterns suitable for the proposed approach. In order to test the results, we also analyze microwave spectral observations during the flare for an estimate of the coronal magnetic field in flare loops, where other radio-emission parameters (number and power-law energy dependence of non-thermal electrons) are constrained by analysis of hard X-ray spectra obtained simultaneously. We describe the observations in Section 2 and give a multi-wavelength overview of the flare in Section 3. The measured quantities are analyzed in Section 4 to estimate the coronal magnetic field separately from the MHD properties and the hard X-ray and microwave emissions. We conclude in Section 5.

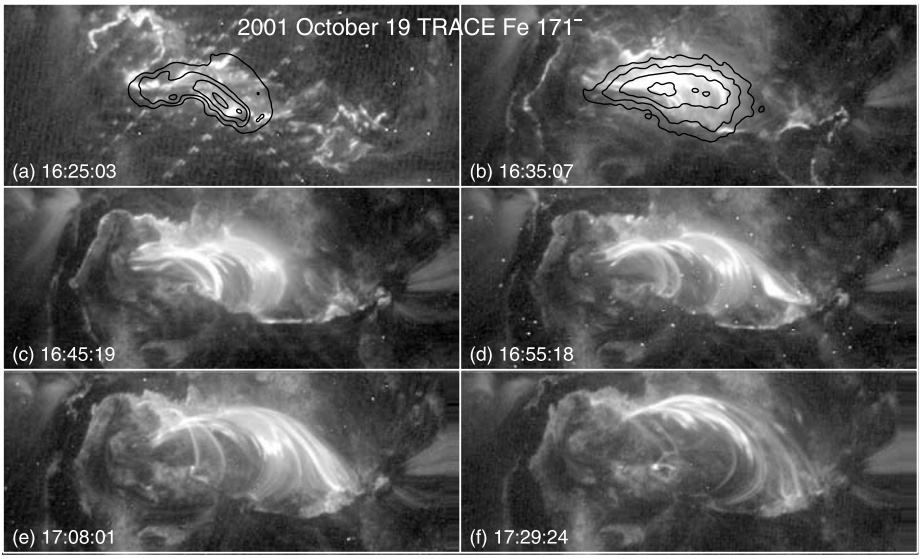

Figure 1 Evolution of the flare at EUV 171 Å by TRACE. The contours in the top panels indicate soft X-ray emission observed by *Yohkoh*/SXT at 15:42:41 (pre-flare) and 16:35:07 UT, respectively.

2. Observations

An X1.6 flare occurred in the active region NOAA9661 (N16W37) on 19 October 2001. TRACE (Handy *et al.*, 1999) observed this event at the EUV 171 Å line with a cadence of 30 – 45 seconds from 16:00 to 18:00 UT for the entire duration of the flare. Figure 1 shows a temporal sequence of the flare–arcade evolution observed by TRACE. These images are analyzed to study the evolution of the flare.

Hard X-ray observations were obtained by *Yohkoh* with the Hard X-ray Telescope (HXT: Kosugi *et al.*, 1991) from 16:20 UT to 16:40 UT and the Wide Band Spectrometer photon counter (WBS; Yoshimori *et al.*, 1991) for a longer period. In this paper, X-ray observations by HXT at four energy channels are analyzed to obtain the energy distribution of non-thermal electrons. To understand the flare-loop evolution, X-ray images in the L channel with photon energy 14 – 23 keV are constructed with the MEM algorithm built into Solar Software.

Magnetograms taken by the Michelson Doppler Imager (MDI; Scherrer *et al.*, 1995) were obtained to study the magnetic properties of the active region. The TRACE EUV images were co-aligned with MDI by registering features such as plage with an accuracy of $\approx 2''$. Hard X-ray images are co-aligned with MDI magnetograms and TRACE EUV images with an accuracy of $\approx 5''$, which is the typical size of the hard X-ray sources.

The microwave observations of this flare were obtained by the Owens Valley Solar Array (OVSA; Gary and Hurford, 1990) at 22 frequencies from 1 to 15 GHz with a two-second cadence. Microwaves beyond 10 GHz are usually emitted by trapped non-thermal electrons spiraling around magnetic-loop field lines. In this paper, we analyze the microwave total power spectra during the flare, in conjunction with hard X-ray spectral analysis, to estimate the mean magnetic field of flare loops.

3. Overview of the Flare

As shown in Figure 1, EUV observations reveal thin, bright flare ribbons from the start of the flare, which rapidly spread apart. Ribbon brightenings are followed by EUV loops that become visible five to ten minutes later. Into the decay phase of the flare, EUV loops show up at increasing altitudes. Observations of the flare evolution in this wavelength alone are consistent with the generally-accepted standard flare picture (see Figure 1 in Forbes and Acton, 1996, and references therein), in which bright ribbons outlining the foot points of flare loops are a consequence of heating of the upper-chromosphere or transition region by either thermal conduction or non-thermal beams generated at the coronal reconnection site and deposited in the lower atmosphere nearly instantaneously via the newly-closed field lines. On the other hand, flare loops seen in coronal lines are formed as a consequence of chromospheric evaporation in response to the ribbon heating. In particular, loops seen at EUV wavelengths in the decay phase are flare loops that have cooled from X-ray-emitting temperatures. The apparent expansion of flare ribbons in the chromosphere or transition region, and rising flare loops in the corona, are considered to be signatures of successive magnetic reconnection at progressively-growing altitudes in the corona, in a more or less organized manner. Therefore, EUV observations for this flare are studied to understand magnetic reconnection.

Figure 2 gives an overview of this event observed in many wavelengths. Figure 2(a) shows the lightcurves of X-rays at different energies, and microwaves at 6.6 GHz. During the impulsive phase, the non-thermal emission of the flare seen in microwaves and hard X-rays at energies $\geq$20 keV consists of three peaks, hereafter designated as peaks I, II, and III, respectively. These three bursts peak at 16:25, 16:31, and 16:43 UT, respectively.

In Figure 2(b), contours of X-ray sources of photon energy 14 – 23 keV are superposed on the EUV images showing flare loops and ribbons. The overlay suggests that the 14 – 23 keV X-ray emission is from flaring loops with the emission maximum located at the loop top. The image sequence further suggests that the X-ray loop-top source is systematically evolving over peak I from 16:23 to 16:28 UT and peak II from 16:30 to 16:34 UT. Such motions can be regarded as the projection of the loop top moving upward, as suggested by the rising flare loops seen in Figure 1. We interpret the rising EUV loops as post-flare loops that have cooled to emit at EUV wavelengths, while the X-ray images depict emission by loop-top sources believed to have formed immediately after the magnetic reconnection.

The flare exhibits bright ribbons in the lower atmosphere, as shown in Figure 1. These ribbons quickly expand during the impulsive phase of the flare. From the sequence of EUV images, we locate the fronts of three well-formed ribbons. Figure 2(c) shows the trajectories of these ribbon fronts superposed on a snapshot image of the flare. The ribbon expansion begins at the start of the flare and lasts throughout the impulsive phase until 16:50 UT.

4. Magnetic Field in Flare Loops

4.1. Magnetic Reconnection Rate

This flare illustrates a traditional two-ribbon configuration, making it a viable candidate to measure, by employing a 2.5D model, the magnetic reconnection rate in terms of the macroscopic reconnecting electric field $E_{\rm rec} = V_{\rm r} B_{\rm r}$, $V_{\rm r}$ being the ribbon expansion velocity and $B_{\rm r}$ the normal component of the magnetic field swept up by the expanding ribbon (Forbes and Priest, 1984). It is imperative that the measured $V_{\rm r}$ reflects the ribbon expansion in the

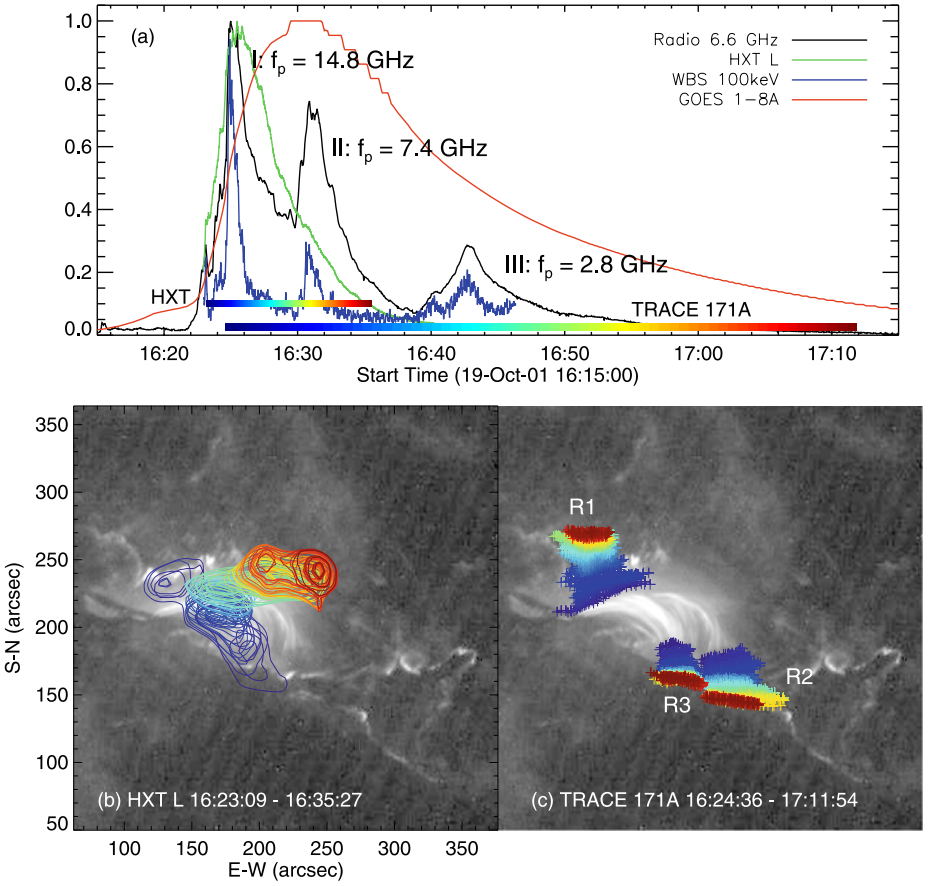

Figure 2 Overview of the flare at several wavelengths. (a) X-ray and microwave light curves. (b) Snapshot of the flare at 171 Å superposed with time sequence of the X-ray source (contours). (c) Snapshot of the flare at 171 Å superposed with trajectories of flare ribbons. The color codes indicate the time lapse which is illustrated in panel (a).

2.5D configuration so that the equation can be used appropriately. Only the velocity component perpendicular to the polarity-inversion line, or the length of the ribbon, provides valid measurement of $E_{\rm rec}$. The velocity component along the polarity inversion line, or along the ribbons, reflects a different aspect of magnetic reconnection and does not enter the equation to compute $E_{\rm rec}$. In this sense, a general $V_{\rm r}B_{\rm r}$ measurement is not meaningful. On the other hand, measuring the total reconnected flux as described in Section 1 is universally valid and, by relaxing the 2.5D requirement, can be applied to a general configuration in addition to two-ribbon flares (Forbes and Lin, 2000; Qiu and Yurchyshyn, 2005; Saba, Gaeng, and Tarbell, 2006; Qiu *et al.*, 2007).

For this flare, however, Qiu *et al.* (2004) evaluated the magnetic reconnection rate by approximating the ribbon evolution to a 2.5D model. In short, we tracked the outer edge of ribbon sections that best reflect a 2.5D motion pattern, as shown in Figure 2(c), and obtained the average speed of the expansion motion of each of the three ribbons, $V_{\rm r}$, and the mean magnetic-field strength $B_{\rm r}$ swept by the ribbon instantaneously, thus deriving $E_{\rm rec} = V_{\rm r}B_{\rm r}$ (Qiu *et al.*, 2002, 2004). The time profile of the mean values of the electric field inferred from

different parts of the ribbons was given by Qiu *et al.* (2004) and reproduced in Figure 3(a), showing that the reconnection rate in terms of $E_{\rm rec}$ is temporally correlated with high-energy emission in hard X-rays and microwaves. In this flare, all three hard X-ray and microwave emission peaks are identified in the $E_{\rm rec}$ profile. This result suggests that $E_{\rm rec} = V_{\rm r} B_{\rm r}$ is a good token of the rate of energy release.

4.2. Motion of Loop Top X-ray Source

As noted earlier, the rising loops (Figures 1 and 2(b)) in conjunction with the regular separation motion of the ribbons in the lower atmosphere (Figure 2(c)) are thought to be a signature of progressive magnetic reconnection described in the standard flare model. The formation and heating of flare loops is a direct consequence of magnetic reconnection, and the magnetic flux is conserved from the loop top to the foot point along the newly formed loops. Therefore, on average, we can write $\langle V_{\rm r} B_{\rm r}\rangle \approx \langle V_{\rm t} B_{\rm t}\rangle$ to reflect this flux conservation, $V_{\rm t}$ and $B_{\rm t}$ being the apparent rising velocity and magnetic field at the top of newly formed flare loops, respectively. With this simple relation between apparent motion and magnetic field at the loop top and foot point, the mean magnetic field at the top of flare loops can be estimated by tracking the loop-top motion, the ribbon expansion, and magnetic field at the foot-point.

In Figure 3(b), we plot the spatial evolution of the loop top X-ray source. The x and y coordinates are derived for the centroid of the loop top source with respect to a reference point $x_0 = \sum(x_i \times C_i)/\sum C_i$ and $y_0 = \sum(y_i \times C_i)/\sum C_i$, where x_i, y_i and C_i are the x and y coordinates and data counts in the ith pixel, and the integration is over those pixels with data counts larger than a cutoff value. We used eight sets of cutoff values of 0.3, 0.4, 0.5, 0.6, 0.7, 0.75, 0.8, 0.85 to derive x_0 and y_0, and plot the mean of these eight sets at each time. Then we fit $x_0(t)$ and $y_0(t)$ to a linear function of time to derive the velocity V_x and V_y. The total velocity is given as $V_t = (V_x^2 + V_y^2)^{1/2}$. Since, during stages I and II, the motion patterns are apparently different, we fit the two stages separately. From the fits, the projected loop-rising velocity is 35 ± 2 and 36 ± 5 km s^{-1} for the two stages, respectively.

Using the data in Figure 3(a) and (b), we can estimate the mean magnetic field at the top of newly formed flare loops as $\langle B_{\rm t}\rangle \approx \langle V_{\rm r} B_{\rm r}\rangle / \langle V_{\rm t}\rangle = \langle E_{\rm rec}\rangle / \langle V_{\rm t}\rangle$. Averaged over peak I, $\langle E_{\rm rec}\rangle$ is 4 V cm^{-1} and $\langle V_t\rangle$ is 35 km s^{-1}, thus $\langle B_t\rangle$ is approximately 120 G. For peak II, $\langle E_{\rm rec}\rangle$ is 2 V cm^{-1} and $\langle V_{\rm t}\rangle$ is 36 km s^{-1}, yielding $B_{\rm t} \approx 60$ G. Note that these values of the magnetic field strength are averaged over a certain range of altitudes.

Note that in estimating $V_{\rm t}$ we do not correct projection effects nor the possibility that the $V_{\rm t}$ derived above also includes the apparent motion along the arcade rather than simply upward. The projection effects would lead to an under estimate of the real $V_{\rm t}$, and the displacement of the reconnection site along the arcade would give rise to an over estimate of $V_{\rm t}$. As these two effects partly cancel each other, without knowing the exact 3D geometry of the flare arcade, we do not make corrections to these effects in this study. The estimated mean magnetic field strength is therefore only accurate to within a factor around one.

We also remark that, judging from the spatial evolution of the flare, magnetic reconnection during peaks I and II takes place in different parts of the arcade. Therefore, the sharp change in x-position from the end of burst I to the start of burst II likely reflects a displacement of the reconnection site between the two stages, hence is not considered as a rising "motion" of the same arcade. Instead, bursts I and II are likely emitted by spatially different loop-top sources, as also reflected in Figure 2(b). However, over each peak, the magnetic reconnection proceeds in a regular pattern, thus validating our calculation of the mean $V_{\rm t}$ over each stage.

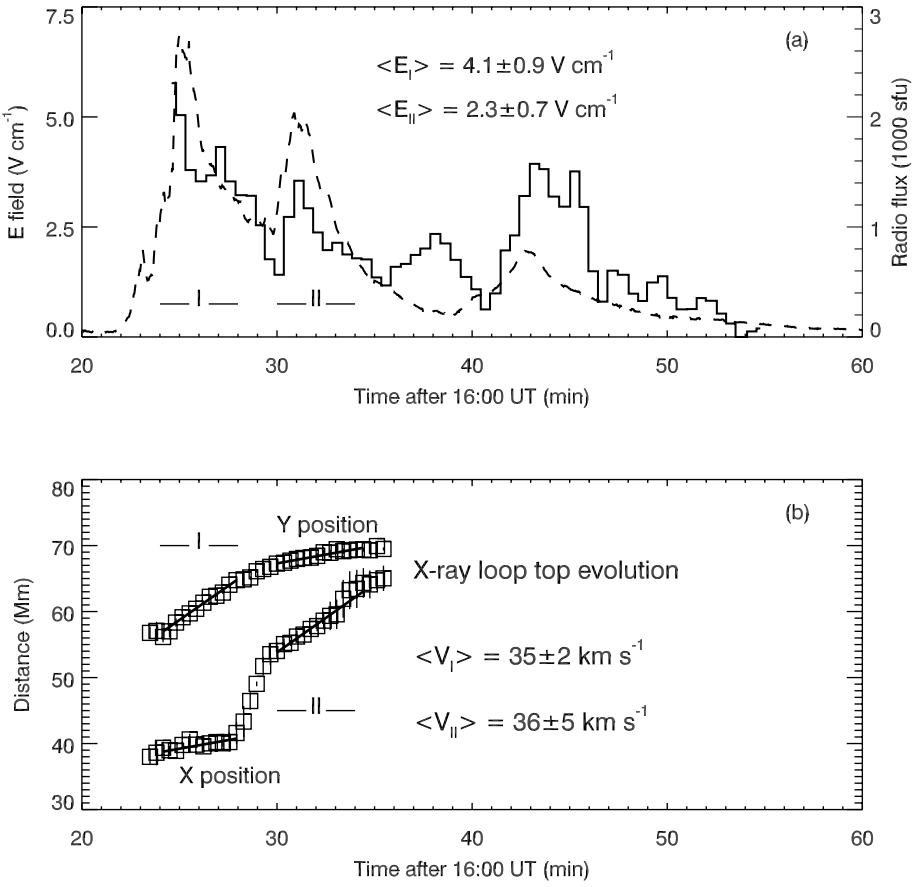

Figure 3 (a) Measurements of mean reconnecting electric field inferred from the ribbon expansion motion (solid lines) with the radio temporal profile (dashed curve) at 6.6 GHz overlaid for comparison after Qiu *et al.* (2004), copyright the American Astronomical Society. (b) Measurements of the spatial evolution of the X-ray loop-top source observed in the HXT L channel (14 – 23 keV).

4.3. Microwave and Hard X-ray Spectral Analyses

A complementary estimate of the magnetic field in the flare loop may be achieved by analyzing the hard X-ray and microwave observations. Non-thermal electrons in a magnetic field produce gyrosynchrotron (GS) emission at microwave frequencies with a spectral peak frequency ($\nu_{\rm p}$) that strongly depends on B. The flux-density spectrum both above and below the peak falls off roughly as a power law (*e.g.* Dulk, 1985; Nita, Gary, and Lee, 2004). The optically-thick GS spectrum below the peak is significantly affected by source inhomogeneity, and hence lacks direct diagnostic power. The spectral peak frequency and flux density and slope of the optically-thin GS spectrum above the peak, on the other hand, do carry important diagnostic information. These parameters are related to the total number ($N_{\rm R}$) and spectral index ($\delta_{\rm R}$) of non-thermal electrons emitting microwaves, the size and location (*e.g.*, the viewing angle θ) of the emitting source, and the magnetic field strength (B) of the source region.

In this paper, we use the method developed by Bastian, Fleishman, and Gary (2007) and Altyntsev *et al.* (2008) to explicitly fit the observed microwave spectrum around and above the peak frequency with a GS source function, and find the magnetic-field strength (B) of the source region from the best fit. We also use as many observational constraints as possible to minimize the number of free parameters in the fitting or to define the range of free parameters. In particular, we analyze hard X-ray spectral observations to derive the spectral index and number density of non-thermal electrons emitting hard X-rays. Note that these electron parameters are not directly used in fitting the GS spectrum, since microwave-emitting electrons are known to be more energetic (Nitta and Kosugi, 1986) and with perhaps different spectral parameters than those determined from hard X-ray observations (Silva, Wang, and Gary, 2000). Nevertheless, hard X-ray spectral analysis can provide reference values for the GS spectrum fitting. The target parameter, the magnetic field at the source, is obviously left free for the fitting.

We use the following parameters measured, or estimated, from observations. Given the flare location at N16W37, the viewing angle (θ) relative to the magnetic field at which the radio brightness peaks is likely between 40° and 90°. Thus, we select a single value in between, $\theta = 70°$, to perform the forward fitting. Note that the shape of the spectrum is only mildly sensitive to the choice of θ (Dulk and Marsh, 1982; Gary, 1985), and our calculations also confirm that varying θ around 70° does not change the derived numbers noticeably. The radio source depth is given a typical value $L = 10^9$ cm, and we also assume the length of the source is $l \approx 3L = 3 \times 10^9$ cm, noting that this is an X-class flare with extended post-flare arcades (Figure 1). Therefore, the area of the source is $A \sim lL$, and the volume of the cylindrical source is given as $V \sim lL^2$.

We derive parameters of non-thermal electrons by analyzing the hard X-ray photon spectrum, assuming that non-thermal electrons emitting hard X-rays have a power-law distribution with a spectral index δ_X. By constructing images of $\geq$20 keV hard X-rays (McKenzie, 2006, private communication), we find that $\geq$20 keV hard X-rays in this flare are primarily thick-target emissions by precipitating electrons. The thick-target electron flux is then given by $F(E) = 8.42 \times 10^{33}\gamma^2(\gamma - 1)^2\mathrm{B}[\gamma - \frac{1}{2}, \frac{3}{2}]CE^{-\delta}$ (electrons s^{-1} keV^{-1}), where C, γ, and $\delta_X = \gamma + 1.5$ (Silva, Wang, and Gary, 2000) can be found from the hard X-ray photon spectrum fitted to a power-law $I(\epsilon) = C\epsilon^{-\gamma}$ (photons cm^{-2} s^{-1} keV^{-1}).

Using HXT multiple-channel observations with appropriate calibration (Sato *et al.*, 1998), we obtain C and γ from a look-up table that relates the ratio of hard X-ray counts in different channels to the spectral index. We then calculate $F(E_0) = \int_{E_0}^{\infty} F(E)\,\mathrm{d}E$ (electrons s^{-1}) at the cutoff energy E_0. In the present study, we choose $E_0 = 100$ keV, because microwaves are primarily emitted by high-energy electrons (Nitta and Kosugi, 1986). Figure 4 shows the temporal profiles of γ and F(100 keV). It is seen from the figure that at peak I, $\gamma \approx 4$, and $F(100\ \mathrm{keV}) \approx 2.5 \times 10^{34}$ s^{-1}, while at peak II, $\gamma \approx 3.5$, and $F(100\ \mathrm{keV}) \approx 2. \times 10^{33}$ s^{-1}. Note that for peak II, only M2-H count rates are used, because in the M1 channel (23 – 33 keV), peak II is overwhelmed by the decreasing emission of peak I. For peak I, we estimate γ using both M2-H data and M1-M2-H data, yielding a difference smaller than 0.5, which we take as the uncertainty in determining γ. Uncertainty in estimates of electron number flux is about a factor of two by using different channels, as well as using an empirical scaling relationship by Aschwanden *et al.* (1999).

If the same electrons emit hard X-rays and microwaves, then the total number of electrons emitting microwaves may be estimated to be $N_R \approx F(E_0)\tau(E_0)$ where $\tau(E_0)$ is the lifetime of the 100 keV electrons in the radio source. This life time can be roughly estimated as the delay between hard X-ray and microwave emissions (Gary, 1985). In this flare, there is no evident time delay during peak I and II (see Figure 4) given the cadence (two seconds) of

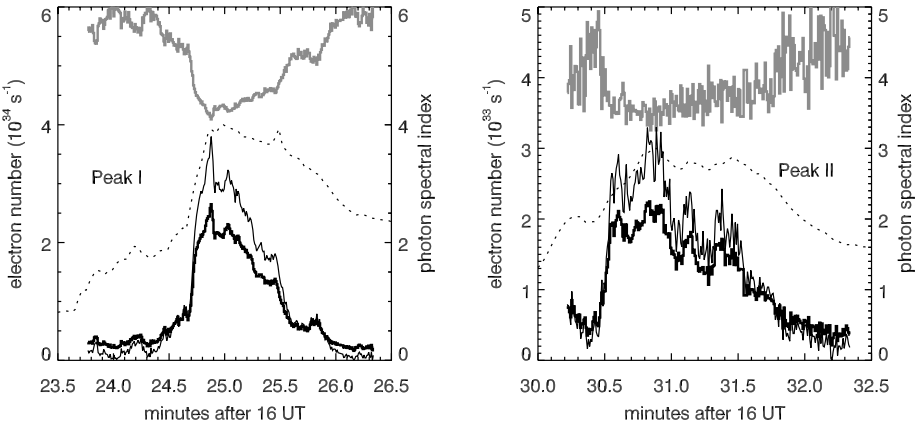

Figure 4 Electron number flux (dark thick solid lines) and photon spectral index (grey thick solid lines) derived from fitting the hard X-ray spectrum obtained by *Yohkoh*/HXT. Also plotted are the hard X-ray count rate light curve at 23 – 33 keV (thin solid lines) obtained by HXT and the microwave flux density at 6.6 GHz (thin dotted lines) obtained by OVSA, both arbitrarily normalized.

microwave observations. Therefore, we take $\tau =$ two seconds as the characteristic lifetime of ≈100 keV electrons. The number density of >100 keV microwave electrons is $n_{100} = N_R/V$. With the set of parameters given above, $n_{100} \approx 2 \times 10^7$ cm^{-3} at peak I and $n_{100} \approx 2 \times 10^6$ cm^{-3} at peak II.

However, it has been understood that the spectral index (δ_R) of trapped electrons emitting microwaves is generally different from δ_X, because microwave-emitting electrons are usually of higher energies. Therefore, in our GS fitting we leave δ_R a free parameter, while the δ_X derived from hard X-ray spectral analysis provides a reference value to compare with the fitting result. The values of n_{100} could be different as well, yet the shape of the GS spectrum is insensitive to even a large change in n_{100} (Dulk and Marsh, 1982). Therefore, in the GS fitting, we use n_{100} values around (by a factor of two) those derived from hard X-ray spectral analysis.

Another quantity, which at times can be important in calculating the GS emission, is the number density of the thermal electrons at the radio source. We note that a decimetric continuum component peaking at about 1.4 GHz is present along with the microwave continuum component. As was demonstrated by Fleishman, Nita, and Gary (2005) and Nita, Gary, and Fleishman (2005), such a decimetric component is often produced by the resonant-transition-radiation mechanism at the local plasma frequency of the radio source cospatial with the microwave source. Therefore, we can estimate the thermal electron density as $n_{th} \approx 2.4 \times 10^{10}$ cm^{-3}. We find that thermal electrons do not significantly affect the GS spectrum during peak I, which is determined by the self-absorption. However, the temporal profile of the peak frequency (see Figure 5(a)) indicates that the GS spectrum during peak II is significantly affected by Razin suppression (Melnikov, Gary, and Nita, 2008). The Razin effect, which is strongly dependent on n_{th}, is taken into account in fitting the microwave spectrum during peak II.

As a result, Figure 5(b) shows the calculated microwave spectrum that best fits the observed spectrum during peak I and II, respectively. The best-fit parameters are $\delta_R = [4.5,\ 3.3]$ and $B = [250,\ 120]$ G for peak I and II, respectively. The best-fit δ_R values indicate that non-thermal electrons at peak II exhibit a harder spectrum than at peak I, as is the case from the hard X-ray spectral analysis, and $\delta_X - \delta_R = 1 - 1.7$, in agreement with

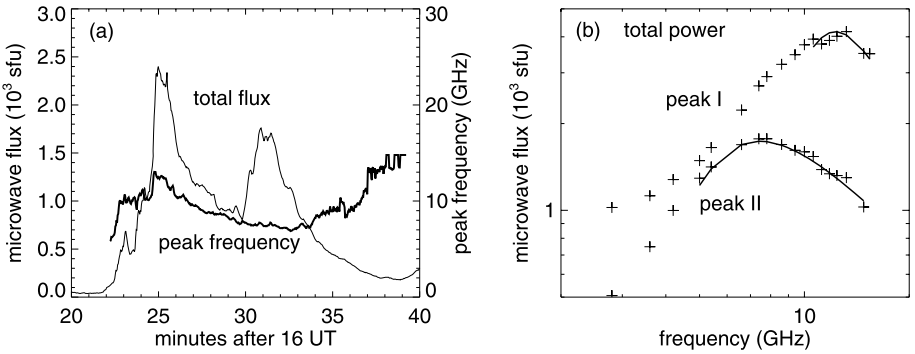

Figure 5 Left: the microwave flux at 6.6 GHz (thin solid line) and peak frequency (thick solid line). Right: the microwave total power spectrum with one-minute integration centered at 16:25:10 UT (peak I) and 16:30:50 UT (peak II), respectively. The thin solid lines show the modeled total power spectra with the best-fit parameters (see Section 4.3).

the statistical results by Silva, Wang, and Gary (2000). Finally, the magnetic field B from the best-fit calculation is consistent with the MHD estimates in the sense that B is smaller during peak II by the same factor of two.

Admittedly, parameters derived from both the X-ray and microwave observations, which we have used to derive B in the two peaks, carry large uncertainties. It is important to understand the robustness of the fitting results. It is well known that higher B values can account for the observed increasing $\nu_{\rm p}$. In addition, B measurement is not too sensitive to variations in $n_{100}L$ and δ. Changes in $n_{100}L$ by three to four orders of magnitude and changes in δ by ± 1 would result in changes in B by no more than 50%. Therefore, even very large uncertainties in determination of the electron number, which is often the case, do not significantly affect the B measurement. Then, comparing the two radio peaks, observations reveal a high $\nu_{\rm p}$ ($>$13 GHz) for peak I and a relatively low $\nu_{\rm p}$ ($<$7 GHz) at peak II. As found from hard X-ray spectral analysis, the electron number varies from peaks I to II by only one order of magnitude, the electron spectral index by $\approx$0.5, and no significant change in the source size or geometry. We expect that these parameters of the microwave emitting source would vary from peak I to II in a similar manner. From the foregoing discussion, it is argued, therefore, that the magnetic field B must be stronger in the source region of peak I by roughly a factor of two, as primarily reflected in the peak frequencies.

5. Discussion and Conclusion

In this paper, we analyze observations of a two-ribbon flare in several wavelength regimes, revealing the temporal, spatial, and spectral evolution of the flare emission in varying depths of the atmosphere. From the apparent expansion motion of flare ribbons in the lower atmosphere, we measure the rate of magnetic reconnection in terms of the reconnecting electric field $E_{\rm rec} = V_{\rm r}B_{\rm r}$. The magnetic-reconnection rate evolves along with hard X-ray and microwave observations, each exhibiting three peaks during the impulsive phase of the flare with an average $E_{\rm rec} \approx 2 - 4$ V cm^{-1}. X-ray imaging observations by *Yohkoh*/HXT also reveals an organized spatial evolution, most likely reflecting the rising loop-top emission source, in company with the ribbon expansion motion, as reconnection proceeds progressively at higher altitudes forming higher flare loops. These apparently rising flare loops are

later visible in EUV wavelengths, having cooled down from X-ray temperatures. Using the conservation of magnetic flux from the corona to the lower atmosphere where the field is rooted, we estimate the mean magnetic field at the top of flare loops by $\langle V_r B_r \rangle \approx \langle V_t B_t \rangle$, yielding $B_t \approx 120$ and 60 G over the emission peaks. An estimate of mean magnetic field in the flare loops is also obtained from microwave and X-ray spectral analysis, yielding $B \approx 250$ and 120 G at the two peaks, respectively. This result is consistent with the estimates of B_t from the MHD measurements, in the sense that magnetic field in flare loops is reduced during the second peak by the same factor of two.

It is noted that the mean magnetic field B_t estimated from motions of flare ribbons and the loop-top source is nearly the lower limit of B measured from microwave spectroscopic observations. This apparent discrepancy may be understood in several ways. First, the mean magnetic field from microwave analysis refers to the total strength, but the first method yields only the horizontal component, $B_t < B$. Second and more importantly, gyrosynchrotron electrons are likely trapped and emit in a larger region than the flare loop top. In this case, the measured B from the gyrosynchrotron spectrum is an appropriately weighted value of magnetic field from the loop top to the loop leg, which should be greater than B_t at the loop top. We also acknowledge that measurements with both methods are estimates with several assumptions. For example, parameters of hard X-ray emitting electrons are derived using observations at only two or three energies below 100 keV. In principle, our spectral analyses and measurements can be improved when high-resolution imaging spectroscopic observations are available in hard X-rays, as is currently possible with RHESSI, and in the future in microwaves with the Frequency Agile Solar Radiotelescope (FASR), whose potential is clearly demonstrated by our experiment in the present study.

Acknowledgements We thank *Yohkoh*, TRACE, and OVSA teams for providing quality observations. JQ is supported by NSF grants ATM-0603789 and ATM-0748428, and NASA grant NNX08AE44G to Montana State University. The OVSA observations are supported by NSF grant AST-0607544 and ATM-0707319 and NASA grant NNG06GJ40G to the New Jersey Institute of Technology. We thank the anonymous referee for constructive comments which help improve the manuscript.

References

Aschwanden, M.J., Kosugi, T., Hanaoka, Y., Nishio, M., Melrose, D.B.: 1999, *Astrophys. J.* **526**, 1026.
Altyntsev, A.T., Fleishman, G.D., Huang, G.-L., Melnikov, V.F.: 2008, *Astrophys. J.* **677**, 1367.
Bastian, T.S., Fleishman, G.D., Gary, D.E.: 2007, *Astrophys. J.* **666**, 1256.
Dulk, G.A.: 1985, *Ann. Rev. Astron. Astrophys.* **23**, 169.
Dulk, G.A., Marsh, K.A.: 1982, *Astrophys. J.* **259**, 350.
Fleishman, G.D., Nita, G.M., Gary, D.E.: 2005, *Astrophys. J.* **620**, 506.
Fletcher, L., Hudson, H.: 2001, *Solar Phys.* **204**, 69.
Fletcher, L., Pollock, J.A., Potts, H.E.: 2004, *Solar Phys.* **222**, 279.
Forbes, T.G., Acton, L.W.: 1996, *Astrophys. J.* **459**, 330.
Forbes, T.G., Lin, J.: 2000, *J. Atmos. Solar-Terr. Phys.* **2**, 1499.
Forbes, T.G., Priest, E.R.: 1984, In: Butler, D.M., Papadopoulos, K. (eds.) *Solar Terrestrial Physics: Present and Future*, NASA, Washington, 35.
Gary, D.E.: 1985, *Astrophys. J.* **297**, 799.
Gary, D.E., Hurford, G.J.: 1990, *Astrophys. J.* **361**, 290.
Handy, B.N., Acton, L.W., Kankelborg, C.C., Wolfson, C.J., Akin, D.J., Bruner, M.E., Caravalho, R., Catura, R.C., Chevalier, R., Duncan, D.W., *et al.*: 1999, *Solar Phys.* **187**, 229.
Isobe, H., Takasaki, H., Shibata, K.: 2005, *Astrophys. J.* **632**, 1184.
Isobe, H., Yokoyama, T., Shimojo, M., Morimoto, T., Kozu, H., Eto, S., Narugake, N., Shibata, K.: 2002, *Astrophys. J.* **566**, 528.
Kosugi, T., Masuda, S., Makishima, K., Inda, M., Murakami, T., Dotani, T., Ogawara, Y., Sakao, T., Kai, K., Nakajima, H.: 1991, *Solar Phys.* **136**, 17.

Lee, J., Gary, D.E.: 2008, *Astrophys. J.* **685**, L87.
Lee, J., Gary, D.E., Choe, G.S.: 2006, *Astrophys. J.* **647**, 638.
Lin, J., Ko, Y.-K., Sui, L., Raymond, J.C., Stenborg, G.A., Jiang, Y., Zhao, S., Mancuso, S.: 2005, *Astrophys. J.* **622**, 1251.
Melnikov, V.F., Gary, D.E., Nita, G.M.: 2008, *Solar Phys.* **253**, 43.
Miklenic, C.H., Veronig, A.M., Vrnak, B., Hanslmeier, A.: 2007, *Astron. Astrophys.* **461**, 697.
Nita, G.M., Gary, D.E., Fleishman, G.D.: 2005, *Astrophys. J.* **629**, L65.
Nita, G.M., Gary, D.E., Lee, J.: 2004, *Astrophys. J.* **605**, 528.
Nitta, N., Kosugi, T.: 1986, *Solar Phys.* **105**, 73.
Poletto, G., Kopp, R.A.: 1986, In: Neidig, D.F. (ed.) *The Lower Atmosphere of Solar Flares*, NSO/Sacramento Peak, Sunspot, NM, 453.
Qiu, J., Yurchyshyn, V.B.: 2005, *Astrophys. J.* **634**, L121.
Qiu, J., Lee, J., Gary, D.E., Wang, H.: 2002, *Astrophys. J.* **565**, 1335.
Qiu, J., Wang, H., Cheng, C.Z., Gary, D.E.: 2004, *Astrophys. J.* **604**, 900.
Qiu, J., Hu, Q., Howard, T.A., Yurchyshyn, V.B.: 2007, *Astrophys. J.* **659**, 758.
Saba, J.L.R., Gaeng, T., Tarbell, T.D.: 2006, *Astrophys. J.* **641**, 1197.
Sato, J., Sawa, M., Masuda, S., Sakao, T., Kosugi, T., Sekiguchi, H.: 1998, *The Yohkoh HXT Image Catalogue*, Nobeyama Radio Obs./Natl. Astron. Obs.
Scherrer, P.H., Bogart, R.S., Bush, R.I., Hoeksema, J.T., Kosovichev, A.G., Schou, J., Rosenberg, W., Springer, L., Tarbell, T.D., Title, A., Wolfson, C.J., Zayer, I., MDI Engineering Team: 1995, *Solar Phys.* **162**, 129.
Silva, A.V.R., Wang, H., Gary, D.E.: 2000, *Astrophys. J.* **545**, 1116.
Temmer, M., Veronig, A.M., Vrnak, B., Miklenic, C.: 2007, *Astrophys. J.* **654**, 665.
Yokoyama, T., Akita, K., Morimoto, T., Inoue, K., Newmark, J.: 2001, *Astrophys. J.* **546**, L69.
Yoshimori, M., Okudaira, K., Hirasima, Y., Igarashi, T., Akasaka, M., Takai, Y., Morimoto, K., Watanabe, T., Ohki, K., Nishimura, J.: 1991, *Solar Phys.* **136**, 69.